IOP Publishing and International Atomic Energy Agency Nuclear Fusion
Nucl. Fusion **50** (2010) 115005 (12pp) doi:10.1088/0029-5515/50/11/115005

# Modelling of Kelvin–Helmholtz instability and splashing of melt layers from plasma-facing components in tokamaks under plasma impact

**G.V. Miloshevsky and A. Hassanein**

School of Nuclear Engineering, Center for Materials under Extreme Environment, Purdue University, West Lafayette, IN 47907, USA

E-mail: gennady@purdue.edu

Received 6 May 2010, accepted for publication 6 September 2010
Published 30 September 2010
Online at stacks.iop.org/NF/50/115005

**Abstract**
Plasma-facing components (PFCs) in tokamaks are exposed to high-heat loads during abnormal events such as plasma disruptions and edge-localized modes. The most significant erosion and plasma contamination problem is macroscopic melt splashes and losses from metallic divertor plates and wall materials into core plasma. The classical linear stability analysis is used to assess the initial conditions for development and growth of surface waves at the plasma–liquid metal interface. The maximum velocity difference and critical wavelengths are predicted. The effects of plasma density, surface tension and magnetic field on the stability of plasma–liquid tungsten flows are analytically investigated. The numerical modelling predicts that macroscopic motion and melt-layer losses involve the onset of disturbances on the surface of the tungsten melt layer with relatively long wavelengths compared with the melt thickness, the formation of liquid tungsten ligaments at wave crests and their elongation by the plasma stream with splitting of the bulk of the melt, and the development of extremely long, thin threads that eventually break into liquid droplets. Ejection of these droplets in the form of fine spray can lead to significant plasma contamination and enhanced erosion of PFCs. The numerical results advance the current understanding of the physics involved in the mechanism of melt-layer breakdown and droplet generation processes. These findings may also have implications for free surface liquid metal flows considered as the first wall in the design of several types of future fusion reactors.

(Some figures in this article are in colour only in the electronic version)

## 1. Introduction

Divertor materials in tokamak devices are expected to face steady-state thermal loads (∼5–20 MW m$^{-2}$) as well as transient heat loads due to plasma disruptions (20–100 MJ m$^{-2}$ with duration 0.1–10 ms) and edge-localized modes (ELMs, ∼1–3 MJ m$^{-2}$ with duration 0.1–1 ms) [1]. Plasma disruptions and ELMs can cause melting and evaporation of metallic plasma-facing components (PFCs) [2–7]. The high melting point, high thermal conductivity, low tritium retention and low erosion rate of tungsten under plasma impact make it very attractive as PFCs. However, macroscopic melt-layer losses may lead to severe damage and unacceptably short lifetimes of the tungsten divertor material [8] and can further lead to serious plasma contamination. It was estimated that the melt-layer thickness of liquefied tungsten is 10–100 times higher than the evaporation losses [4, 6, 7]. The melted metal will remain on the surface forming a thin liquid layer. The macroscopic loss of this melt layer due to plasma impact momentum and/or Lorentz force can significantly contribute to the total amount of erosion crucially affecting the lifetime of PFCs and contaminating the plasma. The core plasma can collapse from this macroscopic tungsten influx in the case of giant ELMs and other abnormal events. Melt-layer removal is governed by the ablation physics of ejected macroscopic material, not by evaporation/ionization physics. These issues are also of concern for future devices with free surface liquid metal flows considered as the first wall. Therefore, a science-based understanding of the physical mechanism of melt-layer losses under plasma impact during the course of disruptions and ELMs is important for the successful development of fusion reactors [7, 8].

A number of laboratory experiments were designed on different devices to study melt-layer formation and its

 

behaviour under the impact of plasma, laser and electron beams. The operating conditions in these facilities may not be relevant to plasma disruption and ELM conditions in tokamaks due to different pulse durations, incident angles, energy depositions, the absence of a magnetic field, etc. However, these experimental facilities are useful for understanding the underlying physics of the plasma–material interactions in the course of plasma instabilities and their interactions with PFCs. In the VIKA simulation facility [9] (power flux $\sim$100 GW m$^{-2}$ with pulse duration $\sim$0.36 ms), the flows of the molten metal, wave-like structure and ejection of droplets were observed for different target materials including tungsten. The presence of a normal magnetic field significantly affected the behaviour of the melt layer suppressing its splashing. Surface cracking was identified as the main mechanism of tungsten damage at heat loads $\sim$15 MJ m$^{-2}$ with plasma pulse durations $\sim$40–50 $\mu$s using the plasma gun MK-200UG facility [10]. Any evidence of traces of melt-layer motion or boiling was not found. The MK-200UG facility is not well suited for a long time standing test of the divertor materials due to the very short duration of the plasma pulse. Tungsten melt-layer erosion due to melt motion driven by plasma pressure was identified in the experiments using the plasma accelerator QSPA Kh-50 with $\sim$250 GW m$^{-2}$ and pulse duration $\sim$0.1 ms [11, 12]. The formation of an erosion crater with large mountains of resolidified tungsten at the crater's edges and droplets of splashed tungsten was observed. QSPA Kh-50 plasma parameters are more relevant to the ITER ELMs and disruptions. MK-200UG experiments were designed to study vapour plasma generation using short pulses, while the splashing of tungsten melt layer with droplet ejection was investigated in the QSPA experiments at energy fluxes of $>$1.5 MJ m$^{-2}$ [13–15]. Recent experiments carried out using the plasma gun facility QSPA-T [16] demonstrated intense droplet ejection for a tungsten melt layer under the normal and oblique plasma impacts with heat loads $\sim$0.5–2.5 MJ m$^{-2}$ and pulse durations $\sim$0.4–0.6 ms. This plasma load condition is relevant to the transients expected in ITER and can be used to test candidate armour materials. The simulation experiments with the plasma gun QSPA Kh-50 also demonstrated recently that tungsten droplets continued to be ejected from the melt for about 10 ms after the plasma impact [17], a phenomenon that has to be explained. The QSPA investigations of the influence of Lorentz force on the melt motion under heat loads of 0.7 MJ m$^{-2}$ during 0.25 ms demonstrated that the tungsten melt is displaced along the force direction with the formation of an erosion crater [18]. The motion of liquid tungsten caused by the Lorentz force in the medium-size TEXTOR limiter tokamak was observed in the direction perpendicular to the magnetic field lines [19–21]. These simulation experiments clearly demonstrated that the external forces such as plasma impact momentum and Lorentz force can cause macroscopic melt-layer motion, splashing and droplet ejection.

The physical behaviour of the melt layer under disruptions and ELMs is not well understood. The stability of melt layers can be affected by many physical phenomena such as various Lorentz forces from thermoelectric effects, caused by currents linked from the plasma, or induced during breakdown, magneto-hydrodynamic effects induced by the melt motion, complex geometry interacting with the melt-layer motion (lips, end of tile or brush, etc). The theoretical analyses and computer modelling of the stability of a liquid metal surface under the plasma impact and/or Lorentz force are very important for understanding the mechanisms of splashing and droplet formation. The term 'splashing' describes different physical mechanisms, which rely mostly on macroscopic momentum transfer from the impacting plasma or any other volumetric force (Lorentz force) to the melt layer. One mechanism for the macroscopic loss of a melt layer can be from development and evolution of Kelvin–Helmholtz (K–H) instability [22]. Perturbations of the plasma–liquid interface and development of waves can be produced by the high-speed plasma flowing along the thin liquid layer. The K–H instability arising at the plasma–liquid interface can later result in liquid droplet formation and these droplets can be splashed into the plasma [23]. The K–H instability develops under certain conditions. The development of K–H instability in application to the melt-layer problem involves the following features: (1) perturbation of the plasma–liquid interface with very large jump in the density across the interface; (2) large surface-tension force at the interface and (3) topological changes of the plasma–liquid interface with possible formation of small and large liquid droplets. One of required conditions for the development of K–H instability is the presence of a velocity difference at the interface between the fluid flows subjected to a shear. A simple phenomenological model was used in the previous studies to roughly estimate the growth of surface waves, droplet formation and melt-layer losses [16, 24]. In the early stage, this linear analysis can be applied which describes the linear growth rate of the K–H instability. When the amplitude of a perturbation reaches 10–30% of its wavelength, the perturbation grows nonlinearly forming the K–H rollups [25]. The linear analysis cannot describe the aspects of the flow that are essentially nonlinear (e.g. the formation of vorticity, the evolution of vortex lines, the collapse of the rib vortices and the formation of droplets). Linear stability theory fails in this nonlinear regime [25] and numerical methods become a viable alternative. However, the computer modelling of the whole process of the development, growth and breakup of the plasma–liquid metal K–H instability was not reported in the literature. It is very challenging to model such a phenomenon because of its complex nature.

In this work, the classical linear stability analysis of the system of coupled hydrodynamic equations of melt and plasma flows is performed by the method of normal modes [22]. The onset conditions for development and initial growth of the K–H instability at the interface between plasma and liquid tungsten are investigated. The generation of surface waves, splashing, formation of liquid metal plumes, ligaments, fingers and droplets dragged by the plasma flow is studied using the commercial code FLUENT [26]. The paper is organized as follows: the classical linear stability theory of plasma–liquid metal flow is presented in section 2. Computational models are discussed in section 3. The results are analysed in section 4.

## 2. Linear instability analysis of plasma–liquid metal flow

The physical picture of the classical K–H instability is that the infinitesimal velocity or density disturbances at the

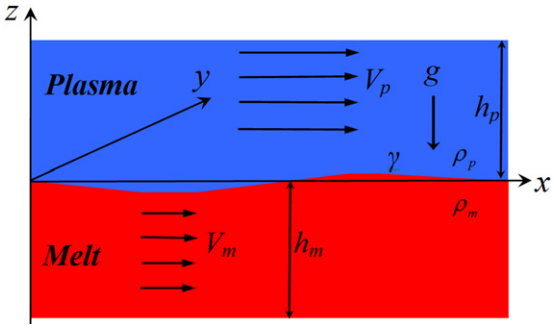


**Figure 1.** Sketch of the parallel flow of plasma and melt streaming, respectively, with velocity $V_\mathrm{p}$ and $V_\mathrm{m}$, of densities $\rho_\mathrm{p}$ and $\rho_\mathrm{m}$, and of interfacial tension $\gamma$. The thicknesses of melt and plasma layers are $h_\mathrm{m}$ and $h_\mathrm{p}$, respectively. Gravity acts in the negative $z$-direction.

melt–plasma interface amplify and grow [22]. The melt is accelerated at the convex regions of the wavy interface and decelerated at the concave regions. These accelerations cause changes in pressure above troughs and over crests so that the resulting pressure differences across the interface tend to amplify the initial disturbances. If the stabilizing effect of the surface tension and gravity is overcome, the interface becomes unstable. A linear analysis of the K–H instability can be found in various textbooks [22, 27, 28]. We follow the analysis of Chandrasekhar [22] applying it to our system shown in figure 1. The parallel flow of homogeneous tungsten melt and plasma fluids of different velocities $V_\mathrm{m}$ and $V_\mathrm{p}$ ($V_\mathrm{p} \gg V_\mathrm{m}$) along the $x$-direction in plane $(x, y)$ of different densities $\rho_\mathrm{m}$ and $\rho_\mathrm{p}$ ($\rho_\mathrm{m} \gg \rho_\mathrm{p}$) with the lighter plasma above is considered. The plasma and melt densities mean the mass of matter per unit volume. The gravity $\boldsymbol{g}$ is perpendicular to the interface and the interfacial surface tension between the melt–plasma fluids is $\gamma$. The plasma velocity is estimated to be in the range $10^4$–$10^5\,\mathrm{m\,s^{-1}}$ [24, 29]. The velocity of melt motion is on the order of $1\,\mathrm{m\,s^{-1}}$. The density of the impacting plasma is $\sim 10^{-7}$–$10^{-6}\,\mathrm{kg\,m^{-3}}$. The parameters of tungsten melt are $\rho_\mathrm{m} = 17\,600\,\mathrm{kg\,m^{-3}}$, $\gamma = 2.5\,\mathrm{N\,m^{-1}}$ [30], and for typical plasma disruptions $h_\mathrm{m} \leqslant 400\,\mu\mathrm{m}$ [20, 31]. The gravity constant is $g = 9.81\,\mathrm{m\,s^{-2}}$. The onset of the K–H instability and critical wavelengths can be analytically predicted by analysing the 3D linearized Navier–Stokes equations [22]. The viscosity terms are usually neglected in this inviscid linear analysis of the phenomena and the Navier–Stokes equations are reduced to the Euler equations. The method of normal modes is then used where small disturbances are transformed into harmonic modes which are treated separately. This detailed and lengthy linear analysis is provided in a textbook of Chandrasekhar [22] for *inviscid* and *infinitely* thick homogeneous fluids. We adapted this inviscid analysis to our system in figure 1 with extension to account for finite thicknesses of melt and plasma layers [32]. The following dispersion relation is obtained

$$\omega = -k_x\left(\frac{\rho'_\mathrm{m}V_\mathrm{m} + \rho'_\mathrm{p}V_\mathrm{p}}{\rho'_\mathrm{m} + \rho'_\mathrm{p}}\right) \pm \sqrt{\left(\kappa g\frac{\rho_\mathrm{m} - \rho_\mathrm{p}}{\rho'_\mathrm{m} + \rho'_\mathrm{p}} + \frac{\kappa^3\gamma}{\rho'_\mathrm{m} + \rho'_\mathrm{p}}\right) - \frac{k_x^2\rho'_\mathrm{m}\rho'_\mathrm{p}}{(\rho'_\mathrm{m} + \rho'_\mathrm{p})^2}(V_\mathrm{m} - V_\mathrm{p})^2}, \quad (1)$$

where $\rho'_\mathrm{p} = \rho_\mathrm{p}\coth(\kappa h_\mathrm{p})$ and $\rho'_\mathrm{m} = \rho_\mathrm{m}\coth(\kappa h_\mathrm{m})$, $\kappa = \sqrt{k_x^2 + k_y^2} = 2\pi/\lambda$ is the real wave number associated with small disturbances proportional to $\exp(\mathrm{i}(k_x x + k_y y + \omega t))$, $\lambda$ is the wavelength, $k_x$ and $k_y$ are the $x$ and $y$ components of the wave number vector $\kappa$, $\omega$ is the (radian) frequency. A detailed derivation of equation (1) for a particular case $h_\mathrm{m} \to \infty$ and $h_\mathrm{p} \to \infty$ can be found in the book of Chandrasekhar [22, p 481]. Its generalization for finite layer thicknesses is provided in [32, p 50]. The relation between $\omega$ and $\kappa$ in equation (1) governs the propagation of capillary and gravity waves on the melt surface. The first term in brackets in equation (1) is the wave velocity represented as the mean, weighted by the densities, of the two fluid velocities. Under the square root in equation (1) the stabilizing forces of gravity and surface tension for, respectively, long and short waves (first two terms in brackets) are balanced by the destabilizing force of inertia (third term). If the expression inside the square root is positive, then disturbance at the interface travels as a wave. For instability, the function under the square root denoted here as $\Theta$ must be negative ($\omega$ has an imaginary part), i.e. the inertial force overcomes the restoring forces of gravity and surface tension. In the case of plasma and melt layers with equal thicknesses, $h = h_\mathrm{m} = h_\mathrm{p}$, equation (1) is reduced to a simplified form [33]

$$\omega = -k_x\left(\frac{\rho_\mathrm{m}V_\mathrm{m} + \rho_\mathrm{p}V_\mathrm{p}}{\rho_\mathrm{m} + \rho_\mathrm{p}}\right) \pm \left[\left(\kappa g\frac{\rho_\mathrm{m} - \rho_\mathrm{p}}{\rho_\mathrm{m} + \rho_\mathrm{p}} + \frac{\kappa^3\gamma}{\rho_\mathrm{m} + \rho_\mathrm{p}}\right) \times \tanh(kh) - \frac{k_x^2\rho_\mathrm{m}\rho_\mathrm{p}}{(\rho_\mathrm{m} + \rho_\mathrm{p})^2}(V_\mathrm{m} - V_\mathrm{p})^2\right]^{1/2}. \quad (2)$$

It follows from equation (1) that the relative velocity must be significantly large to satisfy the following criterion for the K–H instability

$$\Delta V = |V_\mathrm{m} - V_\mathrm{p}| > \sqrt{\frac{\rho'_\mathrm{m} + \rho'_\mathrm{p}}{\rho'_\mathrm{m}\rho'_\mathrm{p}}\left(\frac{G}{\kappa} + \gamma\kappa\right)}, \quad (3)$$

where $G = g(\rho_\mathrm{m} - \rho_\mathrm{p})$ is the gravitational restoring force. We have set $k_x = \kappa$ in deriving equation (3), since the disturbances in the $x$-direction are most sensitive to the K–H instability [22]. For $h = h_\mathrm{m} = h_\mathrm{p}$, equation (3) can be simplified to

$$\Delta V = |V_\mathrm{m} - V_\mathrm{p}| > \sqrt{\frac{\rho_\mathrm{m} + \rho_\mathrm{p}}{\rho_\mathrm{m}\rho_\mathrm{p}}\left(\frac{G}{\kappa} + \gamma\kappa\right)\tanh(kh)}. \quad (4)$$

The critical wave number $\kappa_\mathrm{c}$ can be obtained by taking a derivative of the function under the square root on the right-hand side of equation (3) or (4) with respect to $\kappa$ and equating it to zero. This critical wavenumber $\kappa_\mathrm{c}$ corresponds to the minimum relative velocity required to generate the K–H growing waves. By minimizing the stability function $\Theta$ (under the square root of equation (1) or (2)) with respect to $\kappa$, one can obtain the wavenumber $\kappa_\theta$ corresponding to the fastest growing 'dangerous' wave. However, the analytical formula for $\kappa_\mathrm{c}$ and $\kappa_\theta$ cannot be derived due to the complexity of expressions (1)–(4). The nonlinear algebraic equation originating from the minimization has to be solved numerically in order to determine the critical and most unstable wavenumbers.

The thicknesses of melt and plasma layers appear as parameters in equations (1)–(4). In the limiting case of thick layers $\kappa h \gg 1$, the wavelength is much smaller than plasma

and melt thickness resulting in $\tanh(\kappa h) \sim 1$. Finding the minimum of the stability function $\Theta$ in equation (2) with respect to $\kappa$ leads to

$$\kappa_\theta = \frac{2\rho_m\rho_p(V_m - V_p)^2}{3(\rho_m + \rho_p)\gamma}. \quad (5)$$

At derivation of equation (5), the gravity term was neglected since we consider very short-length waves compared with the thickness of fluid layers. Assuming $\rho_p \ll \rho_m$, equation (5) transforms to one used in a simplified phenomenological capillary droplet model [16, 24] to estimate the mass loss rate due to droplet ejection. In the case of thick layers $\kappa h \gg 1$, equation (4) has also an analytic solution for $\kappa_c$ of the form $\kappa_c = \sqrt{G/\gamma}$. Substituting $\kappa_c$ into equation (4), we obtain the condition for the velocity difference at which waves start to grow on the surface of a thick melt layer

$$\Delta V_c > \sqrt{2\gamma\kappa_c \frac{\rho_m + \rho_p}{\rho_m\rho_p}}. \quad (6)$$

A classical linear theory of the inviscid K–H instability can be extended to include the effect of a magnetic field on the plasma–liquid metal flows. This generalization was performed by Chandrasekhar [22, p 507]. The magnetic tension force can additionally suppress the K–H instability and reduce its growth rate when the magnetic field is parallel or anti-parallel to the direction of the plasma–liquid metal flow. The stabilizing effect of a magnetic field is equivalent to the effect of surface tension with the replacement of $\gamma$ in equation (1) or (2) by $\gamma + \gamma_H$ [22, 28]. Here

$$\gamma_H = \frac{\mu H^2}{2\pi}\frac{k_x^2}{\kappa^3} \quad (7)$$

is the magnetic surface tension, $H$ is the magnetic field and $\mu$ is the magnetic permeability. However, the magnetic field perpendicular to the direction of flow (directed along the $y$-axis in figure 1) has no effect on the unstable waves [22]. The influence of a finite but small viscosity on the growth of the K–H instability is not yet fully understood. It was pointed out that K–H type waves cannot exist in viscous flows: '*including viscous effects, however small, into the stability problem rules out the possibility of the essentially inviscid Kelvin–Helmholtz instability*' [34]. Even small viscosity is important in the boundary layer. In the case of the two fluids with very different viscosities as in plasma–liquid metal flow (hydrogen plasma viscosity $\sim 5 \times 10^{-5}$ Pa s [35] and molten tungsten viscosity $\sim 7 \times 10^{-3}$ Pa s [36]), the onset of the K–H instability is governed by the interplay between viscosity and inertia in the boundary layer [37]. Splashing of the molten layer can also be affected by the adhesion force of the crater bottom with the stabilizing influence. The mass and heat transfer across the interface can reduce the growth of the K–H instability [38]. However, it is found that the stability of the K–H flow is little influenced by the thickness of vapour cloud when the streaming velocity is very large [38]. This overview of physical processes involving the complex interaction of inertial, aerodynamic, magnetic, surface tension and viscous forces demonstrates all the complexity of the formation and growth of waves at the interface between the plasma and liquid tungsten.

## 3. Modelling of two-fluid plasma–liquid metal flows

The plasma and liquid tungsten are treated as the two immiscible fluids of various densities. They are separated by a sharp interface. This two-fluid flow is modelled as a composition of the two pure fluids everywhere, where away from the interface the flow contains only one fluid. The fluids do not mix on the molecular level. A composite consists of small elements of the two pure fluids. Thus, the two fluids keep their own pure-fluid microscopic behaviour. The volume fraction is defined as a scalar indicator function between zero and one that is used to distinguish between two different fluids. A value of zero indicates the presence of one fluid and a value of unity indicates the second fluid. On a computational mesh, volume fraction values between these two limits indicate the presence of the interface and the value itself gives an indication of the relative proportions occupying the cell volume. Typically the volume fraction in the pure plasma $\alpha_p \sim 1 - \varepsilon$, and in the pure liquid $\alpha_m \sim 1 - \varepsilon$ with $\varepsilon \sim 10^{-8}$. The volume fractions satisfy the saturation constraint $\alpha_p + \alpha_m = 1$. This approach is called the volume of fluid (VOF) model [39]. The continuous flow of plasma and liquid metal is governed by the equations which express the conservation of mass and momentum. A single momentum equation is solved and the volume fraction of one of the fluids (plasma) is tracked throughout the computational domain solving the continuity equation. The liquid metal volume fraction is computed from the above constraint. This method requires no further treatment of the interface since it implicitly follows from the flow solution. The interface appears as a smooth transition from one fluid to the other. In the VOF approach, a single-field pressure and velocity are assumed for both plasma and liquid metal. The velocity field is assumed to be continuous at the interface, but the pressure undergoes a jump at the interface due to the surface tension. As the density of plasma is a constant, a continuity equation for the volume fraction of the plasma is given by

$$\frac{\partial\alpha_p}{\partial t} + \nabla\cdot(\alpha_p \boldsymbol{V}) = 0, \quad (8)$$

where $\boldsymbol{V} = (V_x, V_z)^T$ is the single velocity field. The liquid metal volume fraction is then computed as $\alpha_m = 1 - \alpha_p$. The incompressible Navier–Stokes equation can be written as

$$\rho\frac{\partial \boldsymbol{V}}{\partial t} + \nabla\cdot(\rho\boldsymbol{V}\boldsymbol{V} - \eta(\nabla\boldsymbol{V} + (\nabla\boldsymbol{V})^T)) = -\nabla p + \boldsymbol{F}_\sigma + \rho\boldsymbol{g}, \quad (9)$$

where $p$ is the single-field pressure, $\rho$ and $\eta$ are the volume-fraction-averaged density and viscosity, respectively, and they depend on the densities and viscosities of each fluid as $\rho = \alpha_p\rho_p + \alpha_m\rho_m$ and $\eta = \alpha_p\eta_p + \alpha_m\eta_m$. The surface-tension effect is modelled using the continuum surface force (CSF) method [40]. This method transforms surface tension into an equivalent volumetric force. The surface-tension force can be expressed as $\boldsymbol{F}_\sigma = \sigma\zeta\rho\boldsymbol{n}/(0.5(\rho_p + \rho_m))$, where $\sigma$ is the surface-tension coefficient, $\boldsymbol{n} = \nabla\alpha_p$ is the surface normal defined as the gradient of $\alpha_p$ and $\zeta$ is the interfacial curvature. The surface-tension force is proportional to the average mass. In the CSF formalism, the curvature of the surface shape, $\zeta = -\nabla\cdot\hat{\boldsymbol{n}}$, is calculated from local gradients at the interface with $\hat{\boldsymbol{n}} = \boldsymbol{n}/|\boldsymbol{n}|$ is the unit surface normal vector.

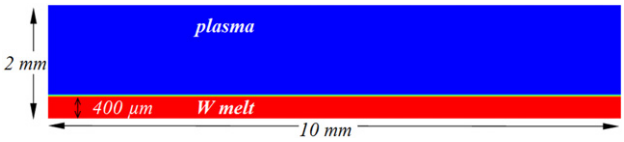


**Figure 2.** Sketch of the computational domain ($(x, z)$-plane) used in the simulation.

The two-fluid plasma and liquid metal flows are considered incompressible, since estimates of the Mach numbers show that they are rather less than 0.3. Thus, the speed of mass waves is much slower than the speed of sound justifying the assumption of incompressibility. The vaporization of tungsten at the plasma–liquid interface is neglected. It is assumed that the thermal energy is not exchanged between the flows, so the energy equation is not solved in this case.

The pressure-based approach [41] is used to model incompressible flows. The velocity field is calculated from equation (9). Equations (8) and (9) are manipulated to derive a pressure correction equation from which the pressure field is extracted. The velocity field is then corrected by this pressure to satisfy the continuity equation. Thus, the computation involves iterations until the solution converges. To satisfy the continuity and momentum equations more closely during iterations, the Pressure-Implicit with Splitting of Operators (PISO) method is used [42]. Neighbour corrections are performed additionally in the PISO algorithm to improve the convergence. Equations (8) and (9) are discretized into algebraic form using a finite volume formulation. Equation (9) is initially discretized using the first-order discretization scheme, but the Monotone Upstream Schemes for Conservation Laws (MUSCL) [43] is applied after several time steps significantly improving spatial accuracy and reducing numerical diffusion. The PREssure STaggering Option scheme [44] is applied to the pressure correction equation to compute the face values of pressure from the cell values. Equation (8) is discretized using a modified version of the High Resolution Interface Capturing (HRIC) scheme [45]. The HRIC scheme provides improved accuracy, robustness and stability for the VOF calculations. This interface-capturing approach does not require additional reconstruction steps, and equation (8) is solved consistently with equation (9). The resultant systems of scalar equations are solved by an algebraic multi-grid method [46]. The plasma–melt flow simulations were run using the commercial FLUENT program package [26].

A sketch of the 2D geometry of the computational domain is given in figure 2. The domain involves the free surface with the interface between the fluids. The two-fluid flow zone is 10 mm long and 2 mm high. The domain's length of ∼10 mm corresponds to the element's length in the tungsten macrobrush [31]. The melt-layer thickness is ∼400 $\mu$m [20, 31]. The FLUENT's preprocessor GAMBIT was used to generate the rectangular 2D geometry and grid with size 400 × 80 cells (mesh size 0.025 mm).

The time step restricted by the Courant–Friedrich–Lewy condition was chosen to be less than $10^{-11}$ s to provide numerical stability. About 20 iterations for each time step are necessary to achieve convergence. The data obtained on a grid with finer meshes appeared to not differ substantially from those obtained with this grid. A decrease in the grid size results in considerably more computational time, data collection and processing. The timescale of computational modelling is limited below 0.1 ms, thus the steady-state regime on the order of seconds cannot be predicted at this time. The periodic boundary conditions are applied in the $x$-direction (figure 1). The top and bottom domain boundaries were modelled as frictionless walls. The top wall is chosen to be far away from the interfacial region of interest in the flow. Volume fractions and densities of two fluids are implemented in the C code as a user defined function (UDF) and used within the FLUENT solver. To initiate the K–H instability, an initial sinus perturbation of the two-fluid interface $\sim a \sin(2\pi x/\lambda)$ with amplitude $a$ and wavelength $\lambda$ was also coded as UDF. The amplitude of perturbation at the interface was within a computational cell.

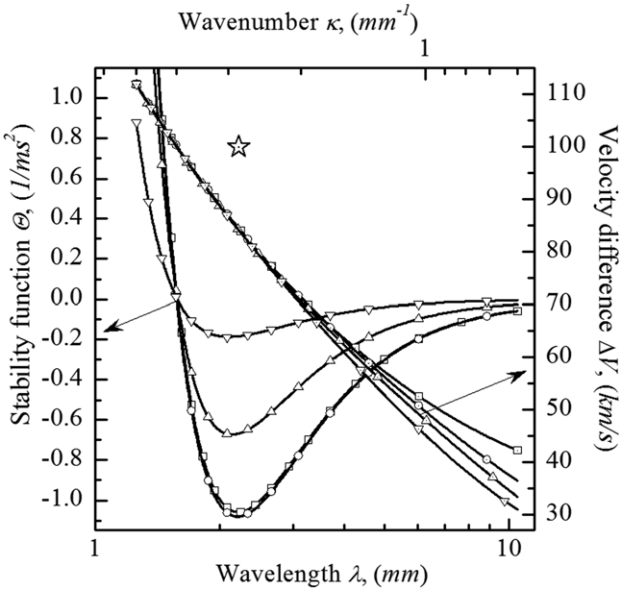


**Figure 3.** Stability function and velocity difference as functions of wavelength, $\lambda = 2\pi/\kappa$, for tungsten melt.

## 4. Results and discussion

In this section we present the results from the linear theory on the onset of the K–H instability and computational modelling of the two-fluid plasma–liquid tungsten flow. The linear analysis is adapted to the dimensions of the system shown in figure 2 in order to compare predictions of the linear stability theory with the computational results.

### *4.1. The onset of the K–H instability from the linear theory*

The stability function calculated from equation (1) and the velocity difference calculated from equation (3) are shown in figure 3 for various combinations of melt and plasma layer thicknesses. The scale of wavenumbers is shown above in this figure. The arrows indicate the axes to which the curves belong. The density of plasma is $10^{-6}$ kg m$^{-3}$. Stability function curves: (1) solid line with squares → $h_m = 400\,\mu$m and $h_p = 1600\,\mu$m; (2) solid line with circles → $h_m = 400\,\mu$m, $h_p = 1600\,\mu$m and $g = 0$; (3) solid line with up triangles

→ $h_m = 200\,\mu$m and $h_p = 1800\,\mu$m and (4) solid line with down triangles → $h_m = 50\,\mu$m and $h_p = 1950\,\mu$m. Relative velocity curves: (1) solid line with squares → $h_m = 400\,\mu$m and $h_p = \infty$; (2) solid line with circles → $h_m = 400\,\mu$m and $h_p = 1600\,\mu$m; (3) solid line with up triangles → $h_m = 400\,\mu$m, $h_p = 1600\,\mu$m and $g = 0$ and (4) solid line with down triangles → $h_m = 1000\,\mu$m and $h_p = 1000\,\mu$m. The star marks the 'dangerous' wavelength (wavenumber) corresponding to the relative velocity $\Delta V = 100\,\mathrm{km\,s^{-1}}$. The range of wavelengths within 10 mm corresponding to the length of the computational domain in figure 2 is considered. The range of wavelengths corresponding to negative values of the stability function describes the unstable region. It is seen that there is no influence of gravity on $\Theta$ for the melt thickness $h_m = 400\,\mu$m (compare the two curves with squares and circles). The curve with $h_p = \infty$ (not shown) has coincided with these two curves meaning that a plasma layer with $h_p = 1600\,\mu$m can be considered as infinitely thick, thus justifying our choice of the thickness of a plasma layer (figure 2) used in the computations. The most unstable 'dangerous' wave corresponds to wavelength $\lambda_\theta \sim 2.2$ mm ($\kappa_\theta \sim 2.86\,\mathrm{mm^{-1}}$). If the initial disturbance of the interface is noisy with all wavelengths present, this fastest growing wave will dominate. With the decrease in melt thickness (curves with up and down triangles) the melt layer becomes more stable. The wavelength of the fastest growing wave shifts towards smaller values. The curves of velocity difference are nearly superimposed in the unstable region (negative values of $\Theta$). They diverge for larger wavelengths (>10 mm) that are not of practical interest here. The gravity does not affect a dispersion curve (compare two velocity difference curves with circles and up triangles). Also, the two curves corresponding to $h_p = \infty$ and $h_p = 1600\,\mu$m are nearly the same. The plasma flow with velocities below these dispersion curves cannot generate amplifying K–H waves. It is seen that the plasma streaming with 90–100 $\mathrm{km\,s^{-1}}$ (marked by star) is required to produce the K–H waves with the fastest growing wavelength.

The stability function $\Theta$ calculated from equation (1) as a function of wavelength (or wavenumber) is illustrated in figure 4 for different values of relative plasma–melt velocity. Let us consider the plasma stream with $\Delta V = 100\,\mathrm{km\,s^{-1}}$. The melt becomes more stable as the velocity difference $\Delta V$ decreases. It is seen that the K–H waves cannot be generated by the plasma flow with velocities <80 $\mathrm{km\,s^{-1}}$ ($\Theta$ becomes positive). However, the melt becomes more unstable as $\Delta V$ increases. The characteristic timescale of melt disruption also decreases, since the absolute value of $\Theta$ increases. The fastest growing waves become those with shorter wavelengths.

Density effects of the impacting plasma on a melt layer with thickness 400 $\mu$m are illustrated in figure 5. The shape of velocity difference curves is the same for a range of plasma densities (figure 5(*a*)). For a given wavelength (say $\lambda \sim 2.2$ mm), $\Delta V$ significantly decreases as the plasma density increases. The unstable K–H waves can be produced on the melt surface by the plasma with $\rho_p = 10^{-4}\,\mathrm{kg\,m^{-3}}$ and streaming with velocity ~10 $\mathrm{km\,s^{-1}}$. Thus, the flow of denser plasma along the liquid tungsten surface causes easier disruption of melt films. This is explained by the fact that larger momentum transfers from the plasma to a melt layer can be achieved by increasing the plasma density.

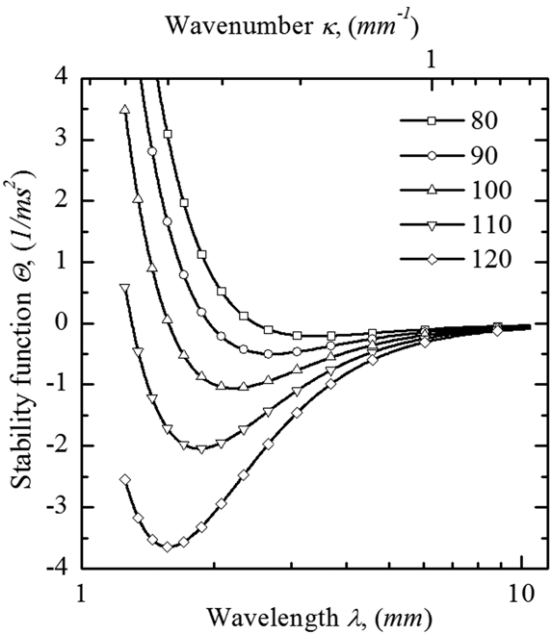


**Figure 4.** Stability function $\Theta$ as a function of wavelength for tungsten melt layer with thickness $h_m = 400\,\mu$m. The plasma thickness is $h_p = 1600\,\mu$m. The curves are shown for various values of velocity difference $\Delta V$ expressed in $\mathrm{km\,s^{-1}}$. The plasma density is $10^{-6}\,\mathrm{kg\,m^{-3}}$.

Let us focus on the velocity difference $\Delta V = 100\,\mathrm{km\,s^{-1}}$ used in our computational modelling. The melt is stable to the flow of plasma with $\rho_p = 10^{-7}\,\mathrm{kg\,m^{-3}}$ (short dashed curve in figure 5(*a*)). Thus, the splashing may not occur for ITER relevant plasma densities ~$10^{19}$–$10^{20}\,\mathrm{m^{-3}}$ and plasma velocities ~100 $\mathrm{km\,s^{-1}}$. As the density of plasma increases by an order of magnitude, the fastest growing wavelength decreases also by an order of magnitude (figure 5(*b*)). It is seen that the plasma with $\Delta V = 100\,\mathrm{km\,s^{-1}}$ and $\rho_p \sim 10^{-4}\,\mathrm{kg\,m^{-3}}$ is needed to excite the most unstable wave with wavelength ~0.04 mm (~40 $\mu$m) used in the droplet model [16, 24]. Figure 5(*b*) shows the imaginary part of $\Theta$ giving an estimate of the temporal rate of wave growth $\Gamma = \mathrm{i}\sqrt{\Theta}$. The characteristic time of the K–H instability can be estimated as $\tau \sim 1/\Gamma$. For the plasma flow with $\rho_p \sim 10^{-6}\,\mathrm{kg\,m^{-3}}$, the K–H instability will develop within $\tau \sim 1$ ms. This is within the melt-layer lifetime. For the plasma stream with $\rho_p \sim 10^{-4}\,\mathrm{kg\,m^{-3}}$, the characteristic time of wave breaking is significantly shorter, $\tau \sim 1\,\mu$s.

The effect of surface tension on the stability of waves is shown in figure 6. The stability function shows that long wavelengths are not affected at all, while the decrease in surface tension has a more destabilizing effect on short-length surface waves. The most unstable wavelength is shifted towards short-length waves. The higher velocity difference is required to disrupt a melt layer with larger surface tension (compare dispersion curves). However, it is seen in figure 6 that variations of surface tension within the range of physical interest [30] seem to have no crucial influence on the critical velocity. For wavelength ~2.2 mm, as the surface tension increases from 2.2 to 2.8 $\mathrm{N\,m^{-1}}$, the critical velocity difference increases by ~10 $\mathrm{km\,s^{-1}}$. Surface-tension effects on the

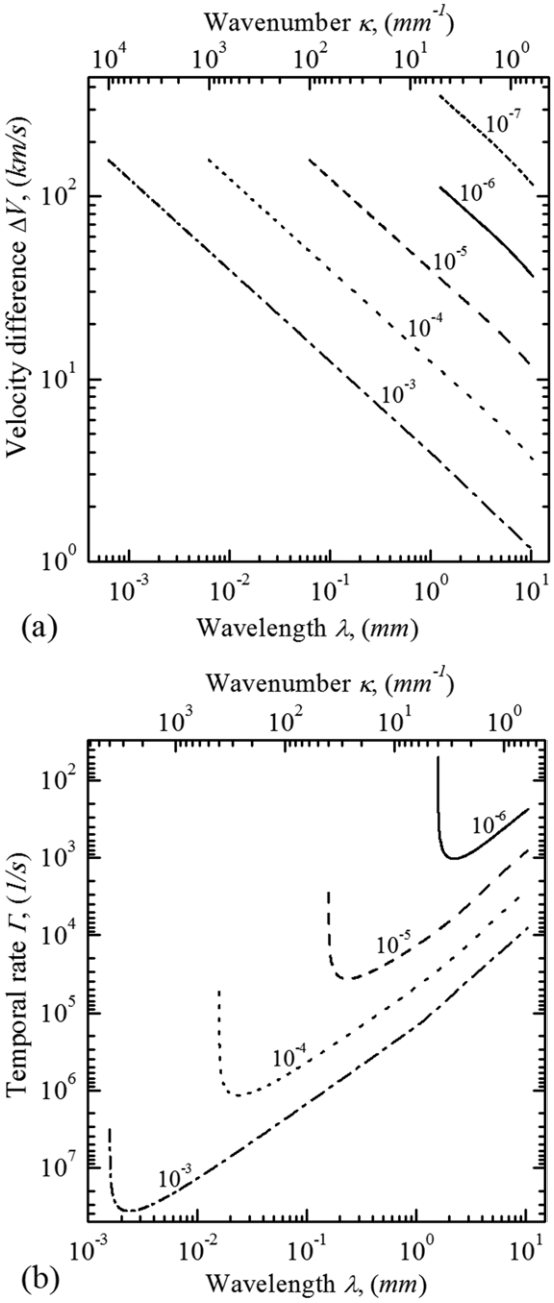


**Figure 5.** Velocity difference (*a*) and temporal rate (*b*) of wave growth as a function of wavelength for tungsten melt layer with $h_m = 400\,\mu$m. The temporal rate of wave growth is shown for $\Delta V = 100\,\mathrm{km\,s^{-1}}$. The plasma thickness is $h_p = 1600\,\mu$m. The curves are shown for different values of plasma density given in $\mathrm{kg\,m^{-3}}$.

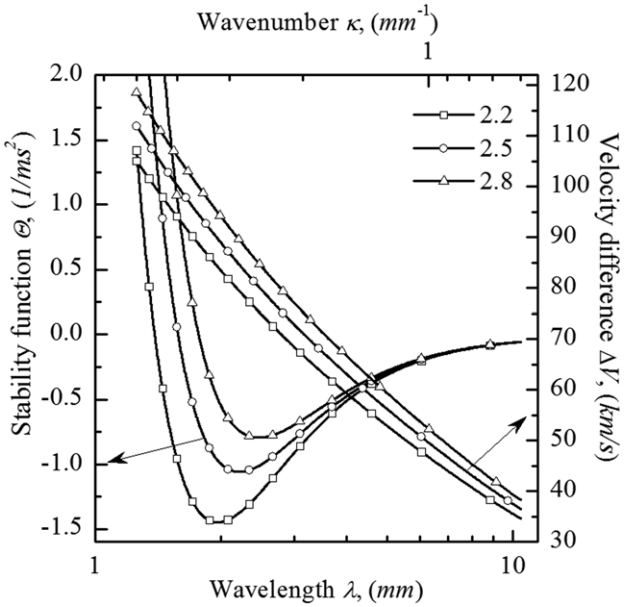


**Figure 6.** Stability function and velocity difference as a function of wavelength for tungsten melt with different values of surface tension given in $\mathrm{N\,m^{-1}}$. The thickness of the melt layer is 400 $\mu$m and the plasma density is $10^{-6}\,\mathrm{kg\,m^{-3}}$. The plasma thickness is 1600 $\mu$m.

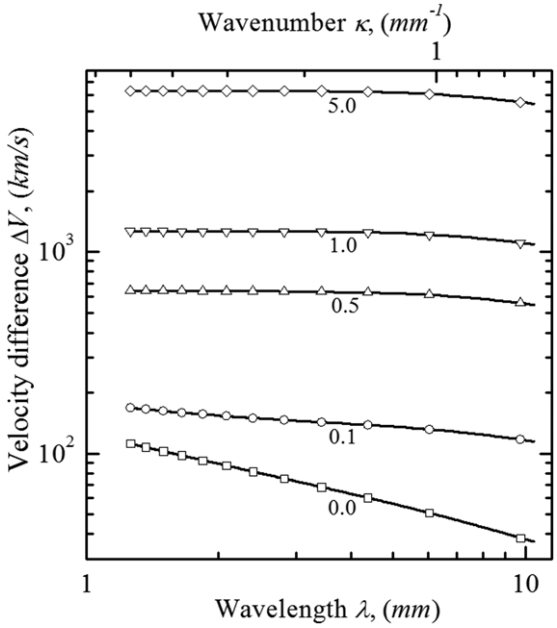


**Figure 7.** Velocity difference as a function of wavelength for tungsten melt at different values of the magnetic field strength in Tesla. The thickness of the melt layer is 400 $\mu$m and the plasma density is $10^{-6}\,\mathrm{kg\,m^{-3}}$.

evolution of the two-phase K–H instabilities were discussed in detail by Zhang *et al* [25].

The magnetic field modifies the surface tension (equation (7)) along its direction. It was determined that surface waves are additionally suppressed by the magnetic surface tension with the magnetic field acting in the flow direction [22, 28]. Figure 7 shows the dispersion curves for different values of imposed magnetic field parallel to the propagation direction of the surface waves. The velocity threshold for the generation of unstable waves increases quickly with the increase in the magnetic field. The whole spectrum of wavelengths is affected. It is clearly seen in figure 7 that the surface waves are suppressed more rapidly when a stronger magnetic field is applied. The stability function does not have the imaginary part at $H = 0.1$ T. For a magnetic field strength of 1 T, the surface disturbances due to the impacting plasma with speeds of $\sim 10^4$–$10^5\,\mathrm{m\,s^{-1}}$ [24, 29] will be very effectively stabilized along the magnetic field

direction. However, a magnetic field perpendicular to the flow direction (directed along the $y$-axis in figure 1) has no influence on surface waves [22, 28]. These predictions from a linear theory of the inviscid K–H instability were confirmed by recent experiments on the propagation and damping of surface waves on liquid gallium [47]. It was found that surface waves are damped only when a horizontal magnetic field is imposed parallel to the flow direction. The interfacial disturbances were suppressed more strongly with increasing magnetic field strength. No damping was observed in these experiments under a perpendicular magnetic field.

### *4.2. Computational modelling of plasma–liquid tungsten flow*

The onset of K–H instability and the most unstable wavelength can be analytically predicted for inviscid flow using the linearized Navier–Stokes equations (section 2). However, the subsequent growth and nonlinear evolution of the K–H instability cannot be described by a linear analysis. The growing dynamics of wave structures with time can only be predicted by simulations. The VOF model implemented in FLUENT was previously thoroughly validated against the Thorpe experimental data on the occurrence of K–H instabilities in a stratified two-fluid flow [33]. The onset of instabilities, the wave speed, the critical velocity difference and wavelength were found in rather good agreement with both linear inviscid theory and Thorpe data. The different air–water and gasoil vapour–liquid flow regimes as predicted by the Baker chart were recently reproduced using the FLUENT code [48]. We have also performed test simulations of K–H instabilities for air–air and air–helium interfaces. The growth and nonlinear evolution of these interfaces with the 'standard' structures of rollers and ribs [25] were observed. Since these results are not of practical interest for melt-layer splashing, we do not present them here.

We studied numerically the flow of two incompressible, inviscid and immiscible plasma–liquid tungsten fluids separated by a sharp interface under the effects of gravity and surface tension (figure 1). The periodic boundary conditions allow a small computational domain (figure 2) to be used for studies of the long time evolution of the overall structure of the two-fluid flow. However, wavelengths larger than the $x$-dimension (10 mm, figure 2) of the computational domain cannot be excited. The plasma and tungsten melt velocities are taken to be $10^5\,\mathrm{m\,s^{-1}}$ and $1\,\mathrm{m\,s^{-1}}$, respectively. The plasma density is $10^{-6}\,\mathrm{kg\,m^{-3}}$. The influence of the surface tension and gravitational force on the flow has been taken into account. The nonlinear growth and evolution of the interface is investigated for initial surface disturbances with various wavelengths. For these flow conditions, a range of wavelengths is unstable (the stability function has an imaginary part) as seen in figure 3. We demonstrate the results of simulations illustrating the most interesting aspects of the splashing mechanism of a melt tungsten layer.

Figure 8 shows the temporal behaviour of the interface from $t = 0$ to 8 $\mu$s with an initial perturbation wavelength of 2 mm (5 wavelengths). Rich variety of topological structures is observed due to the nonlinear evolution. The surface disturbances grow at $t = 0.4\,\mu$s in amplitude producing small liquid tungsten plumes at the wave crests. The development of

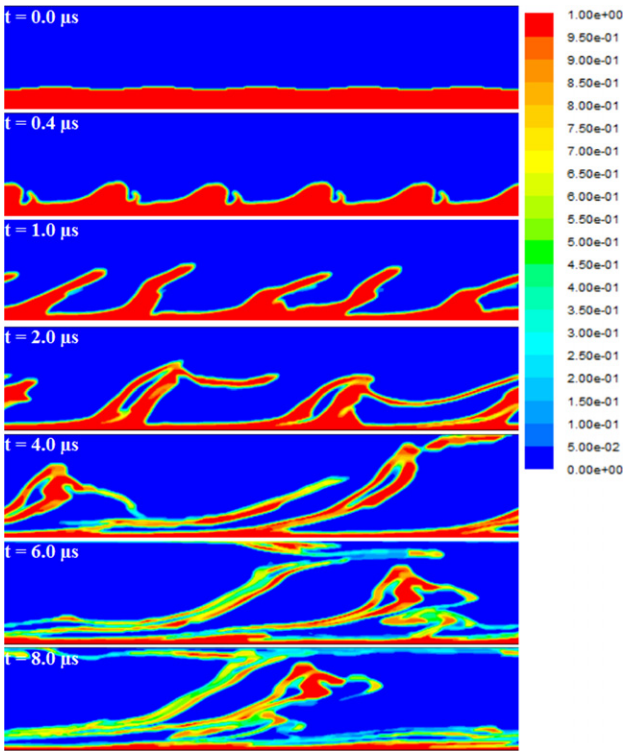


**Figure 8.** Fields of volume fraction for plasma–liquid tungsten flow at different times. Five wavelengths with $\lambda = 2$ mm were initially excited at $t = 0.0\,\mu$s.

a small saw-tooth-like secondary instability is seen. Plumes are elongated further at $t = 1.0\,\mu$s by the plasma flow forming the ligaments. These localized protrusions (ligaments) now have lengths that exceed their widths. Saw-tooth-like secondary instabilities disappear, presumably regularized by surface tension which stabilizes short wavelength disturbances. The interface deforms into elongated liquid tungsten fingers that penetrate into the plasma ($t = 2.0\,\mu$s). The fingers become thinner and curved, as they lengthen. The sides of the fingers collide, thus capturing small pockets of the plasma. For $t \geqslant 4\,\mu$s, figure 8 shows that topological structures of liquid tungsten patterns become highly irregular. Breaks and holes are developed in the melt which are shaped as the open and closed configurations. It is seen that there is a thin continuous liquid tungsten film remaining along the bottom. Melt-layer losses in this case are about 80–90% of the melt thickness. Two other runs performed with zero and inverted gravity have demonstrated no effects of gravity on the development of the K–H instability in agreement with the results from the linear stability analysis (see figure 3).

The initial disturbance of the plasma–liquid tungsten interface with 20 wavelengths (the length of wave is 0.5 mm) at $t = 0.0\,\mu$s is shown in figure 9. According to figure 3 this wavelength is stable. At $t = 5.5\,\mu$s, the original wave crests are smoothed by the tension force which stabilizes the short waves. The plasma-induced tungsten waves show ripply structures without vortices. The interface is stable to disturbances with short wavelengths. From $t \sim 10\,\mu$s, the growing of new waves with larger wavelengths in agreement with predictions from the linear stability analysis is observed.

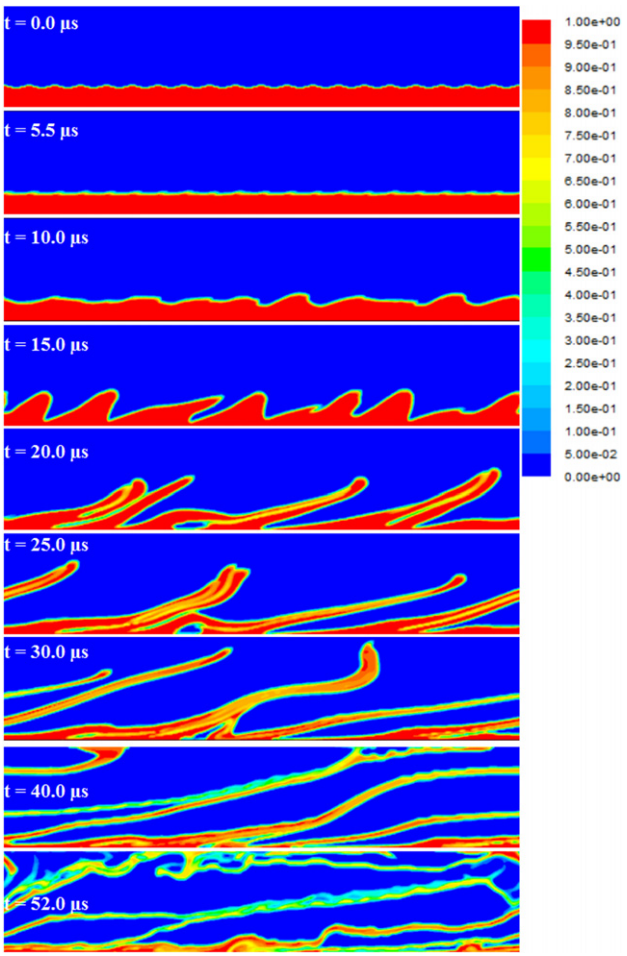


**Figure 9.** Fields of volume fraction for plasma–liquid tungsten flow at different times. Twenty wavelengths with $\lambda = 0.5$ mm were initially excited at $t = 0.0\,\mu$s.

The fastest growing, most dangerous waves self-develop. The wavelength of these bigger wave structures is within ~2 mm. The growth of tungsten plumes as the earliest strongly nonlinear structures is seen at $t = 15\,\mu$s. These plumes split the bulk of the melt layer causing ligaments to form. From $t = 20$ to $30\,\mu$s, elongated ligament protrusions develop well from these liquid tungsten plumes penetrating into the plasma. The interface splits into multiple ligaments with different width. The ligament lengthening is supported by an influx of tungsten from the bottom. The collision of ligaments and their coalescence occurs. Bubbles of plasma trapped during ligament agglomerations become confined within a tungsten melt. The ligaments are partially curved and their lengths are very long (0.5–1.0 cm) at $t = 30\,\mu$s. The formation of long, narrow liquid threads is observed at $t > 40\,\mu$s. As the surface-tension force for tungsten liquid is sufficiently large, the plasma stream only changes the shape of threads creating thinner and thinner segments. The threads still remain surface-bounded. However, these liquid threads are stretched and thinned and eventually can break into droplets. The oscillations of the thread surface due to gravity and surface-tension forces can be the cause for threads to break up into liquid tungsten droplets (see wavy structures in figure 9 at $t \geqslant 40\,\mu$s). Droplet size and number could be estimated from the diameter and length of ligaments. The estimates show that droplet sizes are within the range ~25–200 $\mu$m.

It is found numerically that the most dangerous wave corresponds to ~2 mm (5 wavelengths) for the plasma with density $\sim 10^{-6}$ kg m$^{-3}$ streaming with $\sim 10^5$ m s$^{-1}$. This finding is in agreement with predictions of the linear stability theory (figure 3). The numerical results for 2 and 50 wavelengths are described in [49]. The long waves, ~5 mm, do not grow on the timescale of 0.1 ms. The surface disturbances with 50 wavelengths were also regularized by surface tension. However, short-length disturbances give rise to the growing of new waves with wavelength on the order of ~2 mm. The onset of instability development for longer and shorter waves compared with this range of fastest growing wavelengths is time delayed. When the surface is disturbed with 20 wavelengths (figure 9), the waves start to grow at $t \sim 10\,\mu$s which is significantly slower compared with the case with 5 wavelengths (figure 8). However, no surface waves which amplify to form a periodic array of compact spanwise K–H rollers with conventional K–H finger-like projections that eventually break off to form droplets are revealed in the computational modelling. Instead, relatively long waves (~2 mm) in comparison with the melt thickness (0.4 mm) develop and undergo localized growth with transformations into long ligaments and ribbons that eventually can fragment into liquid droplets. The instability with a wavelength that is typically one to ten times larger than the film thickness is the well-known example [34]. Formation of long ligaments has been observed experimentally in the processes of thin film atomization [50], centrifugal atomization of metal melts [51] and simulations of fingering instabilities [52, 53]. Inspections of metal sample targets exposed to plasma impact in the plasma accelerator QSPA Kh-50 also demonstrate the strip-like structures of melt flow and the streamlets on the non-melted parts of the target with droplets at the ends [11]. Very recent experiments on melt motion and splashing performed in the TEXTOR limiter tokamak showed for the first time the loss of molten tungsten in the form of continuous fine spray with droplets [21]. The strong surface-tension force of tungsten holds the ligament interface together for long times. These features cannot be deduced from the linear theory. The linear analysis focuses on the wavelength with the fastest growing rate, and suggests that the droplet size is proportional to this critical wavelength. This assumption was used in a simple phenomenological model [16, 24, 29] predicting the most unstable wavelength ~40 $\mu$m and a four times smaller radius of droplets ~10 $\mu$m. This droplet model is an extension of the linear stability theory to an essentially nonlinear regime with many assumptions about how droplets can be formed. The main assumptions are (1) the unstable wavelength is always significantly smaller compared with the melt thickness (an approximation of the deep melt (equation (5))); (2) the droplets are formed at the peaks of these short waves dragged away by the plasma flow. This model may work for dense plasmas ($N > 10^{22}$ m$^{-3}$ in QSPA-T), but not relevant for ITER conditions ($N \sim 10^{19}$–$10^{20}$ m$^{-3}$) where the most unstable wavelength is significantly larger than the melt thickness. We can estimate using equation (5) that the hydrogen plasma with density $N \approx 3.5 \times 10^{22}$ m$^{-3}$ and $V_p \approx 10^5$ m s$^{-1}$ (figure 5) is required to generate the surface waves with the most unstable

wavelength $\lambda \sim 40\,\mu$m. For the plasma streaming with the lower speed $<10^5$ m s$^{-1}$, the density is larger. However, the computational modelling has to be performed for this specific case of dense plasma to reveal that droplets with radii $\sim 10\,\mu$m are ejected as predicted by the capillary droplet model. The time of wave breaking was estimated to be below 0.1 ms [16, 24]. However, our figure 5 shows that droplet ejection should happen during significantly shorter times, $\sim 1\,\mu$s. In our work, the nonlinear stage of the K–H instability is entirely modelled using the computational simulations. We find that in a particular case of the plasma with $N \approx 6 \times 10^{20}$ m$^{-3}$ the most unstable wavelength is several times larger ($\sim$2 mm) compared with the melt thickness ($\sim$0.4 mm), and the waves grow as continuous long ligaments. Our simulations show that the waves with wavelengths less than the thickness of the melt layer are strongly suppressed and not growing at all. The tips of short waves ($\sim 40\,\mu$m) have a high curvature, which means that their growth is strongly inhibited by large surface tension of the tungsten melt. The physical mechanism of melt-layer losses deduced from our numerical results is also qualitatively different from that proposed in [16, 24, 29]. No droplets formed at the peaks of the surface waves and entrained by the plasma stream are found. Instead, the bulk of the melt layer undergoes macroscopic motion with development and growth of liquid tungsten ligaments that transform to thin threads and eventually break into droplets.

The simulation results shed light on the physical mechanism of macroscopic melt losses that can lead to significant erosion of metals. It is found that about 80–90% of the melt-layer thickness can be lost due to plasma impact in the form of liquid ligaments (figures 8 and 9). This fraction may be overestimated because the adhesion force stabilizing liquid tungsten near the solid–melt interface was not included in the modelling. The estimates available in the literature for the fraction of tungsten melt removed during the plasma impact are uncertain. Using the 1D thermal-erosion model it was assumed that once the melt layer is formed, the fraction of melt loss for tungsten is about 50% [7, 54]. The experiments with plasma accelerator facilities have also shown that metal erosion is governed by macroscopic melt motion [11]. It was found that melt-layer motion is forced by the plasma pressure and resulting in erosion crater with large mountains. The Lorentz force can significantly enhance the melt motion and erosion. The experiments performed in the TEXTOR tokamak demonstrated that at heat loads $\sim 17$ MW m$^{-2}$ the motion of liquid tungsten produces a deep groove $\sim$1 mm on the plate surface with two tungsten jets moved towards the scrape-off layer plasma [20]. The melt splashing under the Lorentz force in the form of continuous fine spray is observed in the TEXTOR tokamak [21]. These experimental data as well as our computations clearly indicate that plasma pressure and/or Lorentz force affect the bulk of the melt layer leading to its macroscopic motion and metal erosion.

## 5. Summary

In this paper we present the first results concerning the physical mechanism of macroscopic melt-layer losses during plasma disruptions in tokamaks. The focus of this work is on understanding the underlying physics processes involved in the breakdown and erosion mechanism of a thin liquid metal layer formed on PFCs. Computer simulations are presented for the first time of the entire processes of the development, growth and breakup of the plasma–liquid metal interface. The observation of continuous liquid tungsten ligaments, their elongation by the plasma flow and development of long, thin threads that eventually can break into liquid droplets is the main result of this work.

The theory based on the linearized Navier–Stokes equations provides firm grounds for understanding the onset of the K–H instability and most dangerous wavelengths. The inviscid linear stability analysis predicts that the plasma streams with density $\sim 10^{-6}$ kg m$^{-3}$ and velocities of $\sim 10^5$ m s$^{-1}$ can generate the growth of surface disturbances on the thin liquid tungsten melt in a range of wavelengths. The most dangerous wave is predicted. Short waves are stabilized by surface tension. The shorter the wavelength of the disturbance, the stabilizing effect of surface tension is more effective. The linear stability analysis can be firmly used to predict the onset of the K–H instability for transient as well as steady-state operation conditions in tokamaks. However, this linear stability theory breaks down in predicting the interfacial structure with the time, and numerical simulations are only the way for further investigations.

The numerical results advance the current understanding of the physics involved in the mechanism of melt-layer breakdown. The incident plasma momentum is transferred to the melt layer increasing its stress. Not only the surface of the melt is affected, but the stress increases gradually in the bulk of the melt with time. This absorption of high shear stress from the interface to the bulk of a thin melt layer causes melt motion and interface reorganization. Initial disturbances on the melt surface in a range of wavelength spectrum can be induced due to the intensive boiling and vaporization. Only certain waves with the fastest growing rate will amplify, grow and break. We found that very short-length waves are suppressed by the surface tension with the interface nearly flattened. However, new unstable waves emerge with significantly longer wavelengths, quickly grow in amplitude and change their shape. This long-wavelength instability of a thin melt layer sheared by the plasma can be induced by the large stress disturbances in the high-density tungsten liquid. The classical picture of the K–H instability is not observed. Rather than roll over and fall back onto the surface, as usually observed for the conventional K–H waves, we find that their plasma entrainment results in the development of elongated structures at the wave crests. The growth of these liquid protrusions on the melt's surface splits the bulk of the melt layer causing long ligaments and thin threads to develop. Ligaments penetrating into the plasma subsequently break into liquid droplets at late times. The actual behaviour and shape of ligaments may be affected by many other factors (magnetic field, temperature dependence of surface tension, viscosity, adhesion forces, etc) not currently included in the computational modelling. Thus, the bulk of the melt layer initially disintegrates into ligaments and further into liquid droplets. This mechanism of melt-layer breakdown is completely different from the one assuming that the K–H instability is induced by the 'plasma wind' on the surface of the liquid tungsten melt.

The effects of additional physics such as viscosity, heat and mass exchange, melt–solid adhesion forces, crater finite

size and magnetic field were neglected in the numerical simulations. While these effects could certainly influence the structure of the plasma–liquid tungsten flow, the breakdown of a melt layer with splitting the interface into long, thin ligaments is a fundamental feature observed in our simulations. The loss of molten tungsten in the form of continuous fine spray with droplets was also recently observed in the TEXTOR experiments confirming a possibility of this phenomenon. Simulation attempts to include viscosities of liquid tungsten and plasma fluids are failed with the periodic and frictionless wall boundary conditions. The fluid's velocities did not remain constant but reduced significantly due to viscous dissipation at the interfacial surface. The simulations involving the boundary conditions with velocity inlet and pressure outlet will be required. With instability development, the flow regime can change and the interfacial surface can significantly enlarge, which could influence the heat and mass transfer. As surface tension is a function of temperature, surface-tension gradients and thermocapillary Marangoni stresses can induce tungsten flows from hot low surface-tension regions to cold regions of higher surface tension, particularly during longer transient events. Adhesion between liquid and solid tungsten may stabilize the thin melts. The finite size of the melt crater can affect the dynamics of the plasma–melt flow. Simulations can reveal the stabilizing effect of the magnetic field is in agreement/disagreement with the predictions from the linear stability theory. Hence, further works should include these effects on the plasma–liquid flow.

## Acknowledgments

This work is supported by the US Department of Energy, Office of Fusion Energy Sciences. TeraGrid computational resources provided by the NCSA under grant TG-PHY090096. The authors acknowledge the NCSA for providing FLUENT software.

## References

[1] Hirai T., Ezato K. and Majerus P. 2005 ITER relevant high heat flux testing on plasma facing surfaces *Mater. Trans.* **46** 412–24
[2] Hassanein A., Konkashbaev A. and Konkashbaev I. 1994 Erosion of melt layers developed during a plasma disruption *Proc. 18th Symp. Fusion Technol.* **1** 223–6
[3] Hassanein A. *et al* 1997 Modeling and simulation of melt-layer erosion during a plasma disruption *J. Nucl. Mater.* **241–243** 288–93
[4] Hassanein A. and Konkashbaev I. 1999 Comprehensive physical models and simulation package for plasma/material interaction during plasma instabilities *J. Nucl. Mater.* **273** 326–33
[5] Wuerz H., Bazylev B., Landman I., Pestchanyi S. and Gross S. 2001 Macroscopic erosion in tokamak off normal events *Fusion Eng. Des.* **56–57** 397–401
[6] Raffray A.R., Federici G., Hassanein A. and Haynes D. 2002 Dynamic chamber armor behavior in IFE and MFE *Fusion Eng. Des.* **63–64** 597–608
[7] Federici G., Loarte A. and Strohmayer G. 2003 Assessment of erosion of the ITER divertor targets during type I ELMs *Plasma Phys. Control. Fusion* **45** 1523–47
[8] Federici G. 2006 Plasma wall interactions in ITER *Phys. Scr.* **T124** 1–8
[9] Litunovsky V.N., Kuznetsov V.E., Lyublin B.V., Ovchinnikov I.B., Titov V.A. and Hassanein A. 2000 Material response due to simulated plasma disruption loads *Fusion Eng. Des.* **49–50** 249–53
[10] Arkhipov N.I. *et al* 2000 Material erosion and erosion products in disruption simulation experiments at the MK-200 UG facility *Fusion Eng. Des.* **49–50** 151–6
[11] Tereshin V.I., Garkusha I.E., Bandura A.N., Byrka O.V., Chebotarev V.V., Makhlaj V.A., Solyakov D.G. and Wuerz H. 2003 Influence of plasma pressure gradient on melt layer macroscopic erosion of metal targets in disruption simulation experiments *J. Nucl. Mater.* **313–316** 685–9
[12] Garkusha I.E. *et al* 2005 Tungsten erosion under plasma heat loads typical for ITER type I ELMs and disruptions *J. Nucl. Mater.* **337–339** 707–11
[13] Federici G. *et al* 2005 Effects of ELMs and disruptions on ITER divertor armour materials *J. Nucl. Mater.* **337–339** 684–90
[14] Zhitlukhin A. *et al* 2007 Effects of ELMs on ITER divertor armour materials *J. Nucl. Mater.* **363–365** 301–7
[15] Klimov N. *et al* 2009 Experimental study of PFCs erosion under ITER-like transient loads at plasma gun facility QSPA *J. Nucl. Mater.* **390–391** 721–6
[16] Bazylev B., Janeschitz G., Landman I., Loarte A., Klimov N.S., Podkovyrovd V.L. and Safronov V.M. 2009 Experimental and theoretical investigation of droplet emission from tungsten melt layer *Fusion Eng. Des.* **84** 441–5
[17] Garkusha I.E. *et al* 2009 Experimental study of plasma energy transfer and material erosion under ELM-like heat loads *J. Nucl. Mater.* **390–391** 814–7
[18] Garkusha I.E. *et al* 2007 Tungsten melt layer erosion due to $J \times B$ force under conditions relevant to ITER ELMs *J. Nucl. Mater.* **363–365** 1021–5
[19] Sergienko G. *et al* 2007 Erosion of a tungsten limiter under high heat flux in TEXTOR *J. Nucl. Mater.* **363–365** 96–100
[20] Sergienko G. *et al* 2007 Experience with bulk tungsten test-limiters under high heat loads: melting and melt layer propagation *Phys. Scr.* **T128** 81–6
[21] Coenen J.W. *et al* 2011 Tungsten melt layer motion and splashing on castellated tungsten surfaces at the tokamak TEXTOR *Proc. PSI-2010 (San Diego, CA, May 2010) J. Nucl. Mater.* at press
[22] Chandrasekhar S. 1961 *Hydrodynamic and Hydromagnetic Stability* (London: Oxford University Press)
[23] Krieger K. *et al* 2011 Induced tungsten melting events in the divertor of ASDEX Upgrade and their influence on plasma performance *Proc. PSI-2010 (San Diego, CA, May 2010) J. Nucl. Mater.* at press
[24] Bazylev B. *et al* 2007 ITER transient consequences for material damage: modelling versus experiments *Phys. Scr.* **T128** 229–33
[25] Zhang R., He X., Doolen G. and Chen S. 2001 Surface tension effects on two-dimensional two-phase Kelvin–Helmholtz instabilities *Adv. Water Res.* **24** 461–78
[26] Fluent-6.3 2006 *User's Guide* Fluent Inc.
[27] Drazin P.G. and Reid W.H. 1981 *Hydrodynamic Stability* (Cambridge: Cambridge University Press)
[28] Shivamoggi B.K. 1986 *Theory of Hydromagnetic Stability* (New York: Gordon and Breach)
[29] Bazylev B.N. and Landman I.S. 2007 Droplet formation at the W-macrobrush targets under transient events in ITER *Problems At. Sci. Technol.* **13** 35–9
[30] Paradis P.-F., Ishikawa T. and Yoda S. 2005 Physical properties of liquid and undercooled tungsten by levitation techniques *Appl. Phys. Lett.* **86** 041901-3
[31] Bazylev B. *et al* 2008 Behaviour of melted tungsten plasma facing components under ITER-like transient heat loads: simulations and experiments *Fusion Eng. Des.* **83** 1077–81
[32] Ishii M. and Hibiki T. 2006 *Thermo-Fluid Dynamics of Two-Phase Flow* (New York: Springer-Verlag)

[33] Bartosiewicz Y., Laviéville J. and Seynhaeve J.-M. 2008 A first assessment of the NEPTUNE_CFD code: Instabilities in a stratified flow comparison between the VOF method and a two-field approach *Int. J. Heat Fluid Flow* **29** 460–78
[34] Boomkamp P.A.M. and Miesen R.H.M. 1996 Classification of instabilities in parallel two-phase flow *Int. J. Multiphase Flow* **22** 67–88
[35] Bruno D., Capitelli M., Catalfamo C. and Laricchiuta A. 2007 Cut-off criteria of electronic partition functions and transport properties of thermal plasmas *28th ICPIG (Prague, Czech Republic, 15–20 July)* pp 235–7 http://icpig2007.ipp.cas.cz/files/download/cd-cko/ICPIG2007/pdf/1P02-02.pdf
[36] Paradis P.F., Ishikawa T., Fujii R. and Yoda S. 2006 Thermophysical properties of molten tungsten measured with an electrostatic levitator *Heat Transfer-Asian Res.* **35** 152–64
[37] Gondret P. and Rabaud M. 1997 Shear instability of two-fluid parallel flow in a Hele–Shaw cell *Phys. Fluids* **9** 3267–74
[38] Lee D.S. 2005 Nonlinear Kelvin–Helmholtz instability of fluid layers with mass and heat transfer *J. Phys. A: Math. Gen.* **38** 2803–17
[39] Hirt C.W. and Nichols B.D. 1981 Volume of fluid VOF for the dynamics of free boundaries *J. Comput. Phys.* **39** 201–25
[40] Brackbill J.U., Kothe D.B. and Zemach C. 1992 A continuum method for modeling surface tension *J. Comput. Phys.* **100** 335–54
[41] Chorin A.J. 1968 Numerical solution of Navier–Stokes equations *Math. Comput.* **22** 745–62
[42] Issa R.I. 1986 Solution of implicitly discretized fluid flow equations by operator splitting *J. Comput. Phys.* **62** 40–65
[43] Van Leer B. 1979 Toward the ultimate conservative difference scheme: IV. A second order sequel to Godunov's method *J. Comput. Phys.* **32** 101–36
[44] Patankar S.V. 1980 *Numerical Heat Transfer and Fluid Flow* (Washington, DC: Hemisphere)
[45] Muzaferija S., Peric M., Sames P. and Schellin T. 1998 A two-fluid Navier–Stokes solver to simulate water entry *Proc. 22nd Symp. on Naval Hydrodynamics (Washington, DC, 9–14 August)* pp 638–51 http://books.nap.edu/openbook.php?record_id=9771&page=638
[46] Stüben K. 2001 A review of algebraic multigrid *J. Comput. Appl. Math.* **128** 281–309
[47] Ji H., Fox W., Pace D. and Rappaport H.L. 2005 Study of small-amplitude magnetohydrodynamic surface waves on liquid metal *Phys. Plasmas* **12** 012102–13
[48] De Schepper S.C.K., Heynderickx G.J. and Marin G.B. 2008 CFD modeling of all gas–liquid and vapor–liquid flow regimes predicted by the Baker chart *Chem. Eng. J.* **138** 349–57
[49] Miloshevsky G. and Hassanein A. 2011 Modeling of macroscopic melt layer splashing during plasma instabilities *Proc. PSI-2010 (San Diego, CA, May 2010) J. Nucl. Mater.* at press
[50] Yun-zhong L.I.U., Minagawa K., Kakisawa H. and Halada K. 2007 Melt film formation and disintegration during novel atomization process *Trans. Nonferr. Met. Soc. China* **17** 1276–81
[51] Zhao Y.Y. 2004 Analysis of flow development in centrifugal atomization: II. Disintegration of a non-fully spreading melt *Modelling Simul. Mater. Sci. Eng.* **12** 973–83
[52] Craster R.V. and Matar O.K. 2009 Dynamics and stability of thin liquid films *Rev. Mod. Phys.* **81** 1131–98
[53] Saber H.H. and El-Genk M.S. 2004 On the breakup of a thin liquid film subject to interfacial shear *J. Fluid Mech.* **500** 113–33
[54] Kamiya K. *et al* 2007 Edge localized modes: recent experimental findings and related issues *Plasma Phys. Control. Fusion* **49** S43–S6